ACS OMEGA

http://pubs.acs.org/journal/acsodf

Article

"Click" Reaction-Mediated Silk Fibroin-Functionalized Thiol-Branched Graphene Oxide Quantum Dots for Smart Sensing of Tetracycline

Kangkan Jyoti Goswami and Neelotpal Sen Sarma*

Cite This: *ACS Omega* 2023, 8, 21914−21928

Read Online

ACCESS | Metrics & More | Article Recommendations | Supporting Information

ABSTRACT: The abuse of tetracycline (TC) antibiotics causes the accumulation of their residue in the environment, which has an irreversible impact on food safety and human health. In light of this, it is vital to offer a portable, quick, efficient, and selective sensing platform to detect TC instantly. Herein, we have successfully developed a sensor using silk fibroin-decorated thiol-branched graphene oxide quantum dots through a well-known thiol-ene click reaction. It is applied to ratiometric fluorescence sensing of TC in real samples in the linear range of 0−90 nM, with the detection limit of 49.69, 47.76, 55.25, 47.90, and 45.78 nM for deionized water, chicken sample, fish sample, human blood serum, and honey sample, respectively. With the gradual addition of TC to the liquid media, the sensor develops a synergetic luminous effect in which the fluorescence intensity of the nanoprobe steadily declines at 413 nm, while the intensity of a newly emerging peak increases at 528 nm, maintaining a ratio that is dependent on the analyte concentration. The increase of luminescence properties in the liquid media is clearly visible by naked eyes in the presence of 365 nm UV light. The result helps us in building a filter paper strip-based portable smart sensor using an electric circuit comprising a 365 nm LED (light-emitting diode) powered by a mobile phone battery which is attached just below the rear camera of a smartphone. The camera of the smartphone captures the color changes that occur throughout the sensing process and translates into readable RGB data. The dependency of color intensity with respect to the concentration of TC was evaluated by deducing a calibration curve from where the limit of detection was calculated and found to be 0.125 μM. These kinds of gadgets are important for the possible real-time, on-the-spot, quick detection of analytes in situations where high-end approaches are not easily accessible.

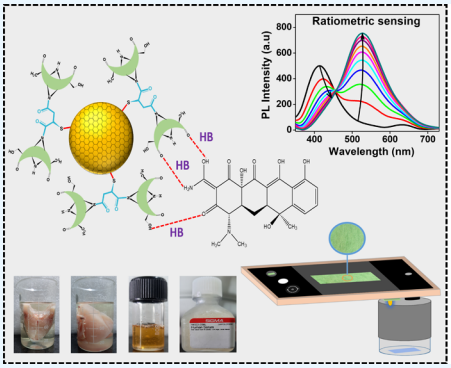

INTRODUCTION

Luminescent nondimensional materials are promising candidates for tremendous applications in the field of photodetectors, solar cells, sensors, and photoelectrocatalytic reactions.[1] Carbon-based materials are excellent candidates for application in the fields of biosensors, bioimaging, and drug delivery due to their excitant biocompatibility and low toxicity.[2] Among them, graphene quantum dots (GQDs) have significant specific surface area, excellent mechanical flexibility, and appealing photostable characteristics. Two-dimensional graphene sheets are often broken up into quantum dot materials using a reducing chemical to remove the oxygen functionalities and decoration on the surface. Due to their nonzero band gap, they show excellent quantum confinement and edge effects.[3] Their potential for use in developing optical sensors and designing smart fluorescent devices for biomedical applications is boosted by their tunable photoluminescence capabilities and their biocompatibility.[4] Moreover, for their unique and versatile properties, they are also tremendously used in other vital applications such as gas biosensors, antigen detection in our body, and so forth.[5−7]

A new type of click chemistry known as hydrothiolation of carbon−carbon double bonds called thiol-ene click reaction has several benefits, such as one-pot synthesis methods with strong regioselectivity and moderate reaction conditions. The interaction with diverse analytes was facilitated by the doping of the sulfur group on the graphitic surface, which produced a large number of active sites connected to the thiol group.[8]

Tetracycline (TC) is a common anti-inflammatory drug extensively used to treat bacterial infections in medicinal industries.[9] It exhibits an effective inhibitory effect on the infections of Gram-positive and Gram-negative bacteria, spirochaetes, ultraviruses, and Rickettsia by preventing the growth of peptide chains and protein synthesis.[9,10] As a consequence, TC is frequently used as a veterinary drug for the

Received: March 15, 2023
Accepted: May 23, 2023
Published: June 6, 2023

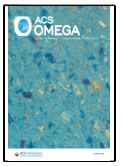

treatment of infections in animals.[11] Long-term usage, however, may result in residual TC in milk, endangering human health by causing problems including anaphylaxis, hepatotoxicity, yellow teeth, nausea, vomiting, liver and kidney damage, and a rise in bacterial resistance to TCs.[9,12−14] Although the antimicrobial effect of TC improved the feed efficiency, the excessive use of TC results in its accumulation in meat products and fish.[15] Moreover, TC is also utilized as a medicinal drug in apiculture to treat extremely contagious bacterial infections like the European and American foulbrood, which mostly afflict and kill bee broads[16] but, adverse effects are observed when the accumulated TC content exceeds the permissible limit of 0.3 mg/kg in the honey sample.[17] Being an organic compound, TC is hard to be degraded naturally, and overusing usually results in the contamination of groundwater, surface water, and drinking water.[18] The Food and Drug Administration (FDA) of the United States has defined the allowable limits for TC in milk products at 900 nM, whereas the European Union has set the permitted limits for the liver at 0.3 mg/kg.[19] Therefore, the identification of TC residue in the contaminated samples is very demanding, concerning the series of adverse effects on animal health. To date, various techniques have been successfully implemented for the detection of TC such as high-performance liquid chromatography (HPLC),[20] LC−mass spectrometry (LC−MS),[21] capillary electrophoresis,[22] immunoassay,[23] electrochemical method,[24] and surface-enhanced Raman spectroscopy.[25] These methods primarily depend on sophisticated instrumentation which are very much time-consuming, difficult to reproduce, expensive, and need professional expertise.[15,21] Moreover, such types of instruments are immobile in nature which significantly limits their performance for the on-spot determination of hazardous chemicals. Therefore, designing effective analytical approaches is indispensable to overcome such disadvantages. Fluorescence-based sensors often acquired great importance due to their simplicity, excellent selectivity, and affordable instrumentation.[9,26,27] Among them, ratiometric fluorescence has quite a significant effect as there exist two signals of opposite intensity that correlate synergistically with respect to the concentration of an analyte. This self-calibration strategy eliminates most of the instrumental impacts and background interferences that primarily affect the selectivity of the sensor.[27−29] Most ratiometric sensing generally operates through common mechanistic pathways such as Förster resonance energy transfer (FRET), inner filter effect (IFE), photoinduced electron transfer (PET), and so forth.[30,31] On the contrary, it was found that when traditional luminophores with delocalized electrons approach a nearby area to form aggregated clusters, they frequently get quenched. At this state, they experience a strong $\pi-\pi$ stacking interaction in the excited state. The rodlike or disk-shaped molecular arrangement favors this interaction because they can easily rearrange to reduce the intermolecular distance.[32] The aggregated state often decays with nonradiative emission. Such "concentration quenching" phenomenon is known as aggregation-caused quenching (ACQ) effect.[33] We observed this ACQ effect along with FRET in our proposed ratiometric sensing system.

Researchers have keen interest in smartphone-based sensor devices due to their great efficiency in detecting colors in a tiny picture region with the help of high-resolution camera modules, big pixel areas, and fast processing speeds.[3,34,35] Moreover, paper-based sensing platforms possess unique characteristics such as portability due to their smaller size and lightweight and cost-effectiveness because of low sample requirements and use of cheaper materials.[36−38] This sensor's working theory is based on the assessment of colorimetric color changes in paper strips coated with a probe material after they interact with the analyte solution and by capturing these images with a smartphone camera, followed by quantization of red, green, and blue color intensities by its application (app).[39] Paper-based materials are biodegradable in nature and are therefore highly ecofriendly.[40,41] This property makes them viable materials for the fabrication of flexible devices and thus of utmost interest toward their usage in the field of biomedical and environmental monitoring applications.[42−44]

In this study, we have synthesized fluorescent quantum dot materials by the functionalization of graphene oxide with thio-malic acid through the thiol-ene click reaction, followed by surface modification with the silk fibroin protein network. The synthesized nanocomposite quantum dot possesses characteristic emission properties which can act as a ratiometric fluorescence sensor toward the detection of tetracycline antibiotics in real samples through a combined effect of aggregation-caused quenching and Förster resonance energy transfer (FRET) pathways. The sensing phenomenon is also monitored by fabricating a paper strip-based portable smart sensor device using mobile phone software and accessories by which changes in the color intensity of filter paper strips can be easily visualized through color channel readout technologies. Moreover, for capturing the images, we have fabricated a prototype of portable mini UV chamber made of cheap nonfluorescent chart paper to reduce the influence of outer light. This kind of smart sensing platform is very demanding concerning food safety and on-site detection of contaminants in real media.

MATERIALS AND METHODS

Materials Used. Graphite powder, sulfuric acid (H_2SO_4), sodium nitrate ($NaNO_3$), potassium permanganate ($KMnO_4$), hydrogen peroxide (H_2O_2, 30%), sodium hydroxide (NaOH), thio-malic acid, *N*,*N*-dimethylformamide (DMF), 2,2-azobis(2-methylpropionitrile) (AIBN), ethanol (EtOH), sodium carbonate (Na_2CO_3), lithium bromide (LiBr), human blood serum, and a dialysis bag with a pore size of 10 kD were purchased from Sigma-Aldrich. All other amino acids and antibiotics were purchased from Sisco Research Laboratories Pvt., Ltd. (SRL Chemicals) and used without further purification. *Bombyx mori* silk cocoons were procured from the mangaldoi silk farm (Darang district, Assam). Whatman filter paper grade 4 (pore size 20−25 μm) and PBS buffer (pH 7.4) were used for the experiments. Other reagents were of analytical grade and used without further purification.

Synthesis of Graphene Oxide. Graphene oxide (GO) is synthesized using a modified Hummer's technique.[45] Initially, 0.25 g sodium nitrate ($NaNO_3$) and 0.5 g graphite flakes were added to a cooled H_2SO_4 solution at 4 °C, and the mixture was stirred for about 20 min. Then, 1.5 g of $KMnO_4$ was gradually added to the mixture, stirring continually and keeping the temperature below 20 °C. The temperature was gradually increased to around 45 °C, after which the solution was stirred for another 90 min, followed by dilution with 50 mL of distilled water under vigorous stirring. A dark brown suspension was formed, in which 6 mL of 30% H_2O_2 solution was added. After that, the mixture was washed numerous times to remove any leftover impurities. The final product was further sonicated for 2 h to obtain exfoliated graphene oxide

https://doi.org/10.1021/acsomega.3c01753
ACS Omega 2023, 8, 21914−21928

Scheme 1. Schematic Presentation for the Preparation of TM-GO-SF QDs

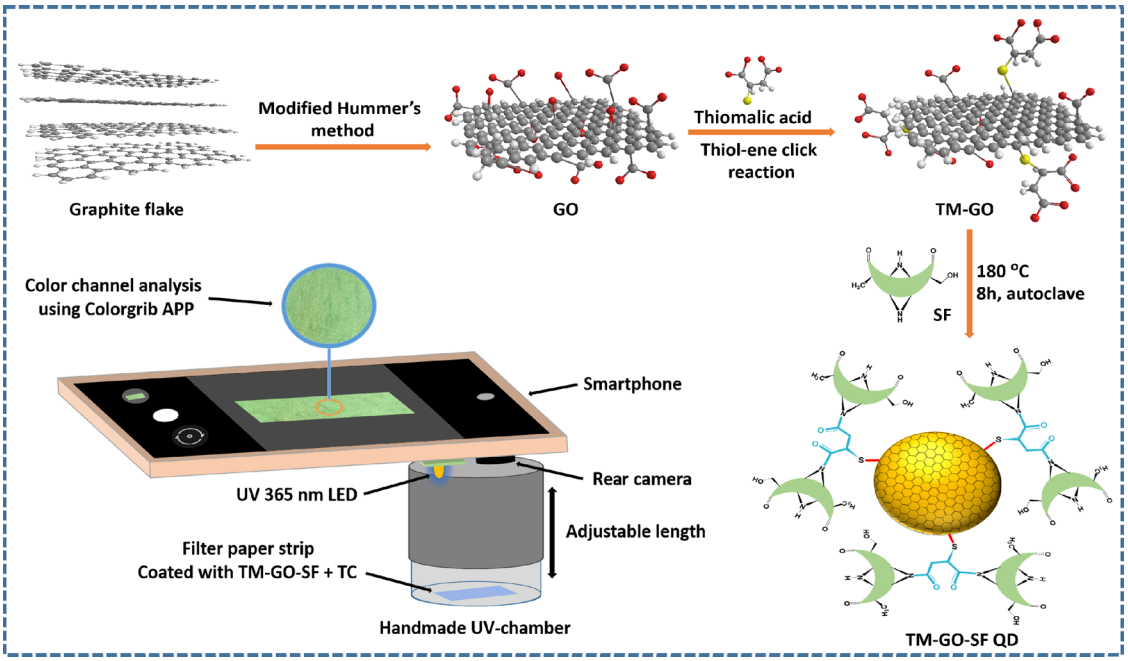

and dried at 60 °C overnight. The purified graphene oxide was stored in a desiccator for future use.

Functionalization of GO by "Thio-ene Click" Reaction (TM-GO). Thiomalic acid-grafted graphene oxide sheets are prepared via thiol-ene Michael addition reaction.[46,47] In this typical procedure, 100 mg of GO was dispersed in 50 mL of *N*,*N*-dimethylformamide (DMF) by using ultrasonication for 1.5 h and transferred to a two-necked round-bottom flask. Initially, N_2 gas was purged for 30 min to create an inert atmosphere. Subsequently, a solution of 2,2-azobis(2-methylpropionitrile) (AIBN, radical initiator) and thiomalic acid in 5 mL of DMF was added dropwise with a continuous bubbling of N_2 gas. The reaction mixture was stirred for 12 h at 70 °C. After cooling down at room temperature, a solution containing ethanol/water (15:5 mL) was added while stirring. The resultant mixture was washed several times with ethanol and water in order to eliminate the impurities. The purified functionalized graphene oxide solution was vacuum-dried to remove the last traces of the solvent.

Extraction of Silk Fibroin from Silk Cocoon. Silk fibroin protein was extracted from silkworm cocoons as in the previously reported method.[48] The silkworm cocoons were first chopped into small pieces and then boiled for 30 min in the presence of aqueous 0.02 M Na_2CO_3 to remove the sericin proteins. After that, the fibers were completely rinsed with ultrapure water and allowed to dry overnight. The dried fibers were dissolved in the prepared 9.3 M LiBr solution (0.1 g/mL) and stirred for 2 h. A dialyzing membrane was used to dialyze the dissolved silk fibroin solution against ultrapure water for 72 h. The SF solution was centrifuged at 4500 rpm after dialysis to remove the debris, and the supernatant was kept in the refrigerator for later use.

Preparation of Silk Fibroin-Decorated Thiol-Branched Graphene Oxide Quantum Dots (TM-GO-SF QDs). Silk fibroin was decoded on the surface of thiomalic acid-functionalized graphene oxide using the following synthesis procedure (Scheme 1). To achieve adequate dispersion, 50 mg of TM-GO was dispersed in 50 mL of deionized water and sonicated for 30 min. 10 mL of SF solution was added to this solution dropwise for 1 h in a N_2 environment under steady stirring. Then, the solution was placed in an autoclave and heated in an oven for 8 h at 180 °C. After cooling to ambient temperature, the solution was transferred to a centrifuge tube, and the separation process was carried out under 10,000 rpm. The upper two-third portion of the solution contained nano-ranged particles and was carefully decanted and stored in the refrigerator for later use.

Fabrication of Cellulose Filter Paper-Modified Paper Strips. A very cost-effective and easiest method for the onsite detection of hazardous analytes is the fabrication of a paper strip-based flexible smart sensor. In the present case, we design an air-stable filter paper strip with surface grafting by TM-GO-SF QDs. Initially, a Whatman filter paper grade 4 was cut into small pieces measuring 3 cm × 1 cm, submerged for 10 s in a solution containing TM-GO-SF quantum dots, and then dried in a vacuum oven for 20 min at 60 °C. Now, the paper strips are ready for use for sensing experiments.

Fluorescence Sensing Method. A ratiometric fluorescence assay was carried out in the presence of PBS buffer (pH = 7.4) to detect TC in aqueous media. In this typical procedure, 500 μL of TM-GO-SF solution was added into a 4 × 1 × 1 cm^3 standard quartz cuvette containing 1 mL of PBS (25 mM pH = 7.4) buffer solution. To this mixture, a definite amount of TC was spiked, followed by filling the cuvette up to 3 mL with deionized water and mixing thoroughly. The sample mixture was excited at 320 nm wavelength, and the corresponding emission spectrum was recorded. On the other hand, to detect TC using cellulose filter paper strip mentioned above, the paper strips were deep in different concentrated solution of TC ranging from 0.1 to 0.9 μM and dried in a vacuum oven at 60° for 20 min. These dried filter papers were then placed in a homemade UV chamber with an adjustable length, as mentioned in the Sensing Mechanism in Results and Discussion.

Instrumentation Techniques. The Fourier transform infrared (FT-IR) measurements were carried out with a

https://doi.org/10.1021/acsomega.3c01753
ACS Omega 2023, 8, 21914−21928

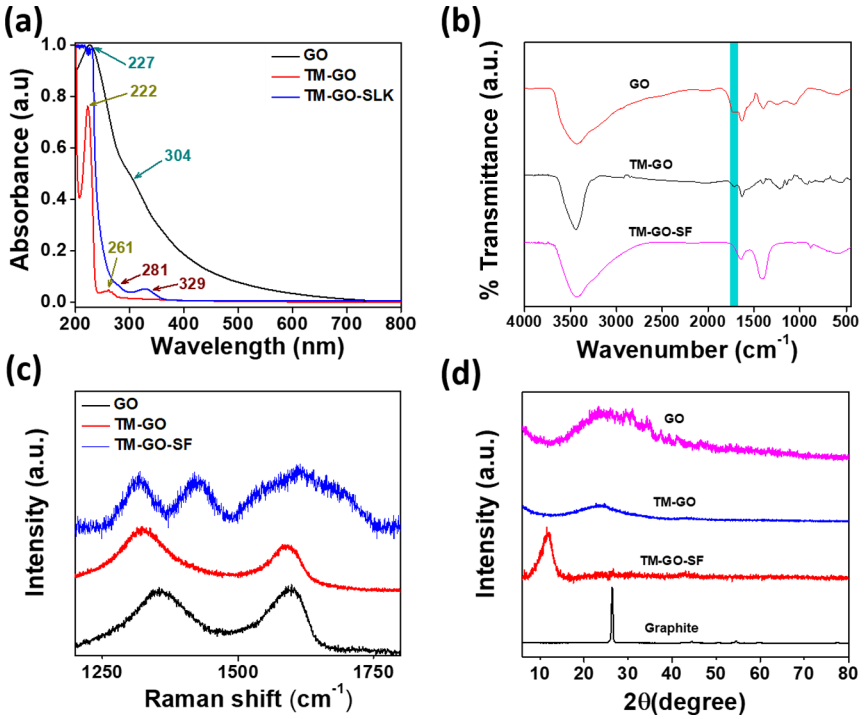

Figure 1. UV−visible spectra (a), FT-IR spectra (b), Raman spectra (c), and XRD patterns of (d) GO, TM-GO, and TM-GO-SF QDs. Comparison of XRD patterns of (d) GO, TM-GO, TM-GO-SF QDs, and graphite.

PerkinElmer FT-IR spectrophotometer utilizing 64 scans, whereas the UV−vis electronic transition experiments were carried out with an 1800 Shimadzu spectrophotometer. A Bruker D8 Advance X-ray diffractometer with a scan rate of 2 s per step was used to observe the XRD patterns with Cu K radiation. It was decided to keep the tube's current, voltage, and angular range at 40 mA, 40 kV, and 2θ = 10−90°, respectively. The fluorescence spectral measurements were performed using a Cary Eclipse spectrophotometer with a 240 nm/s scan rate and a halogen lamp as the excitation source. To ascertain the side and surface charge of the particles, surface zeta-potential and DLS measurements were carried out in a Malvern NanoZS90 system in a glass cuvette with a square aperture and a zeta dip cell electrode at room temperature. The TEM measurement was performed using the JEOL TEM-2100 model by drop-casting on a 3 mm copper grid in order to better analyze the particle size and dispersion. The resulting samples' X-ray photoelectron spectra (XPS) were captured using an ESCALAB Xi+ system (Thermo Fisher Scientific Pvt. Ltd.). Al K was used as the X-ray radiation source, and its excitation energy was 1486 eV. Using a 17 mW laser source with a wavelength of 632.8 nm, Raman analysis was performed using a Horiba Jobin Vyon LabRam Laser micro Raman system, HR model.

RESULTS AND DISCUSSION

Details of the characterization of the as-prepared TM-GO-SF QDs using UV spectroscopy, FT-IR, XRD, Raman, XPS, TEM, and SEM−EDX analyses are discussed below,

Graphene oxide has two distinct absorption peaks at 227 and 304 nm corresponding to the $\pi \rightarrow \pi^*$ transition of C═C bond and $n \rightarrow \pi^*$ transition of C═O bonds, respectively[49] (Figure 1a). After the incorporation of the thiol group on the surface of graphene oxide through the thiol-ene click reaction, $\pi \rightarrow \pi^*$ transition shifted to 222 nm, indicating that π bonds participate in the C−S bond formation process, while $n \rightarrow \pi^*$ transition shifted to 261 nm, emphasizing the availability of more nonbonded electrons from the newly introduced sulfur atoms in TM-GO composites. Furthermore, when TM-GO is further decorated with the silk fibroin protein, the $\pi \rightarrow \pi^*$ transition peak changes from 222 to 281 nm, while the $n \rightarrow \pi^*$ transition shifts to 329 nm, indicating that the graphene sheets in TM-GO composites have been successfully reduced and functionalized by the SF network.[50]

FT-IR spectrum (Figure 1b) of GO exhibits three distinct bands at 1400, 1722, and 3433 cm^{-1}, corresponding to the O−H deformation and C═O and O−H stretching vibrations of carboxylic acid moieties.[51] Furthermore, the alkoxy (RO−) and epoxy (−O−) and C═C groups of GO show stretching vibrations at 1062, 1222, and 1634 cm^{-1}[11]. Two distinct peaks at 2926 and 2858 cm^{-1} are designated as the asymmetric and symmetric vibrations of the CH_2 group, respectively.[52] After completing the functionalization through the thiol-ene Michael addition, the disappearance of the 2500 cm^{-1} peak associated with the common SH group of thiomalic acid reveals that the SH group participates in the formation of covalent linkage with the graphitic C═C bond.[53] Moreover, a prominent peak appears at 1141 cm^{-1}, corresponding to the stretching vibration of the C−S bond, while another peak at 927 cm^{-1} is responsible for the C−S−C semi-ionic stretching vibration.[54] Further surface decoration with the silk fibroin protein leads to the reduction of oxygen-containing groups of TM-GO, which was confirmed by the disappearance of C═O peak at 1717 cm^{-1} and appearance of new peaks at 1640 and 1559 cm^{-1} corresponding to the C═O and N−H stretching vibrational peaks for secondary amide linkage between the thiomalic acid-substituted graphene oxide (TM-GO) and silk fibroin protein.[55,56] This covalent linkage was further confirmed by a broad characteristic C−N stretching vibrational peak at 1408 cm^{-1}.[57]

https://doi.org/10.1021/acsomega.3c01753
ACS Omega 2023, 8, 21914−21928

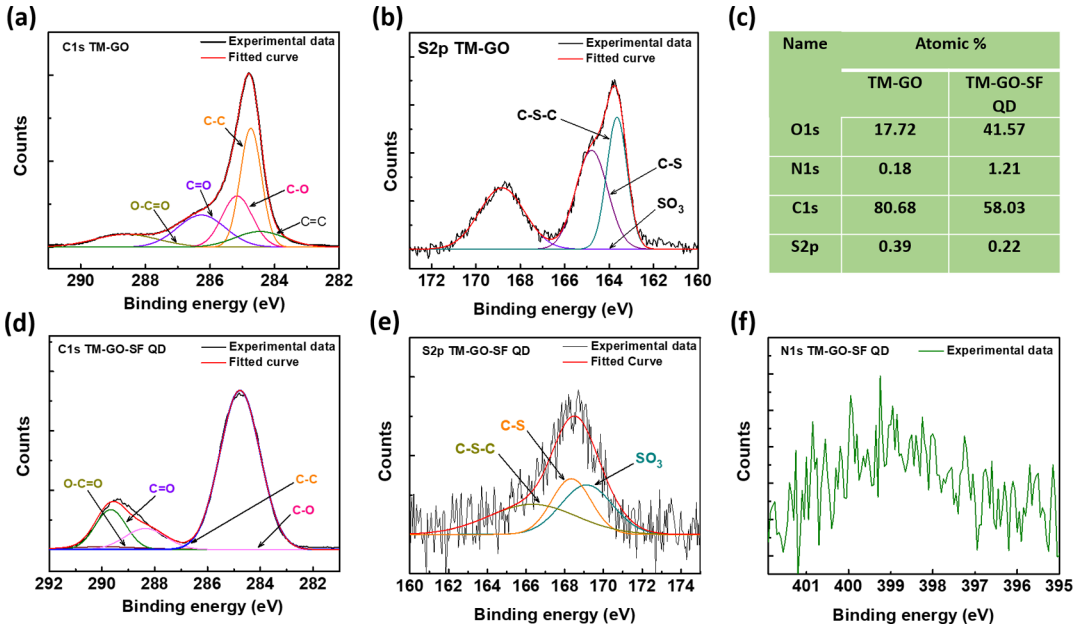

Figure 2. C1s XPS spectra (a) and S2p XPS spectra (b) of TM-GO; atomic % of TM-GO and TM-GO-SF QD (c); C1s spectra (d), S2p spectra (e), and N1s spectra (f) of TM-GO-SF QDs.

Raman analysis is used to evaluate the structural changes, as shown in Figure 1c. Graphene oxide exhibits two distinct bands, namely D band and G band at 1355 and 1596.42 cm^{-1}, respectively.[58] The thiol-ene products of graphene oxide TM-GO shows slightly lower values at 1323.24 and 1591.83 cm^{-1} corresponding to the D and G bands, respectively.[59] Further surface decoration with the silk fibroin protein leads to the shifting of D and G bands to 1318.04 and 1611.99 cm^{-1}, confirming the reduction of oxygen functionalities.[60] The density of sp^2 carbon atoms present in the graphitic network is evaluated by comparing the intensities of D and G bands by taking the intensity ratio I_D/I_G or sp^3/sp^2. This ratio signifies the extent of disorder of the basal plane, which increases significantly from 0.971 to 1.319, emphasizing the distortion of delocalization through the covalent attachment of SH group on the surface of graphene oxide by the thiol-ene click reaction. The reduction of functionalized graphene by silk fibroin protein chains decreases the I_D/I_G ratio to 0.869, which indicates the regeneration of delocalization in the 2D carbon network.[61]

The basic nanostructural organization of all synthesized materials is investigated through XRD analysis, as shown in Figure 1d. Pristine graphene exhibits an intense diffraction peak at 26.390 corresponding to the d-spacing of 3.363. After oxidation by using the modified Hummer's method, this peak shifted to 11.930 with the d-spacing of 7.4095, attributed to the incorporation of oxygen-containing functional groups on the surface of the graphene network. Further functionalization with thiomalic acid results in the shifting of the diffraction peak to 23.76 for the (002) plane mainly due to the removal of oxygenated groups (−OH, −OR) through the incorporation of a bulky thiol group to the C═C bond, as confirmed by the lowering of the intensity of the O−H deformation band and alkoxide stretching vibration at 1400 and 1042 cm^{-1}, respectively, as shown in the FT-IR spectrum of TM-GO.[54] The corresponding d-spacing is found to be 3.7404. Silk fibroin-decorated functionalized graphene shows a diffraction peak at 25.95, clearly emphasizing that the d-spacing of 3.429 for the (002) plane decreases due to further reduction of surface functional groups through the surface-decorating SF network attached by a covalent amide linkage, as shown in the FT-IR spectrum in Figure 1b.

The C1s spectrum of GO displays distinct peaks at 284.3, 285, 287.3, and 288.9 eV, corresponding to C═C, C−C, C−O, and O−C═O bonds, respectively.[62] However, once the SH group is added to the surface of GO by the thiol-ene click reaction, these peaks shift to 284.44, 284.73, 285.16, and 288.59 eV.[54] (Figure 2). The newly introduced S2p spectra of TM-GO clearly show the presence of C−S−C and C−S bonds, as well as SO_3, with binding energies of 163.64, 164.78, and 168.32 eV, indicating the precise grafting of the S atom on the 2D sheet.[63] The surface functionalization of TM-GO with silk fibroin protein causes a noticeable alteration in the C1s spectra, with the binding energies of C−C, C−O, O−C═O, and C═O bonds changing to 284.81, 288.25, 288.55, and 288.25 eV, respectively, as well as an increase in the percentage of N. Figure 2c shows the XPS elemental analysis of TM-GO and TM-GO-SF for C, O, and N. The presence of 0.39 at% S confirms the decoration of S atoms on the graphene sheet surface. In contrast, after effective functionalization with SF, TM-GO sheets were reduced to zero-dimensional quantum dot particles with silk fibroin protein, and the atomic percent of C decreased from 80.68 to 58.03. The chemical composition of the synthesized TM-GO was analyzed through energy-dispersive X-ray (EDX) analysis, as shown in Figure 3. The TM-GO sheet exhibits a significantly detectable peak of S atom of 1.45 wt %, indicating the successful grafting of the thiol group on the surface of GO.

TEM is used to configure the nonstructural conformation of prepared materials, as shown in Figure 4. The thiol-ene product TM-GO has a semitransparent 2D nanosheet with a scrolling structure that includes the characteristic wrinkles around the edge and displays remarkable flexibility with a minimal thickness. After the treatment of the silk fibroin protein, TM-GO sheets undergo complete breakdown to zero-dimensional quantum dots of average diameter 4.66 nm. The

https://doi.org/10.1021/acsomega.3c01753
ACS Omega 2023, 8, 21914−21928

(a)

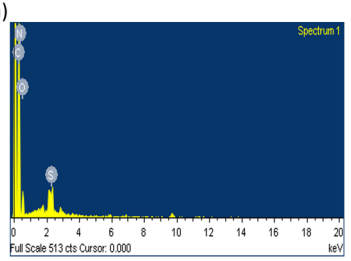

(b)

Element	Weight%	Atomic%
C K	171.53	167.68
N K	-131.73	-110.42
O K	56.28	41.31
S K	3.91	1.43
Totals	100.00	

Figure 3. SEM EDX spectra showing the comparative weightage of different atoms present in thiolated graphene oxide through the thiol-ene click reaction (a) and the corresponding weight and atomic % of elements (b).

decorated layer of SF is clearly visible in the HRTEM images, and it is highlighted with a yellow line (Figure 4d). Moreover, quantum dot particles are composed of layered structures with a lattice fringe spacing of 0.0754 nm. The probability distribution curve for these quantum dots is shown in Figure 4f, emphasizing that the maximum percentage of particles exist with a diameter around 3 nm.

Fluorescence Ratiometric Sensing. Photoluminescence spectroscopy is used to investigate the characteristic changes that occur in the emission spectrum of TM-GO-SF QDs in the presence of varying concentrations of tetracycline.

We excited the nanoprobe at different excitation wavelengths ranging from 290 to 240 nm, and the associated emission spectra are displayed in Figure S1. The nanoprobe shows a maximum emission at 413 nm on excitation at 320 nm, which undergoes a bathochromic shift to 528 nm in the presence of tetracycline (TC). When we start the measurement with a 10 nM concentration of TC, the emission spectrum of the nanoprobe shows a considerable decrease in fluorescence intensity at 413 nm (I_{413}) while a significant increase in the region of 528 nm (I_{528}). On further increasing the concentration of the analyte by 10 nM at a time up to 90 nM, the I_{413} value goes on decreasing while the corresponding I_{528} value successively increases (Figure 5a). At a higher concentration of the analyte, the change of intensity for both these regions is quite small compared to their lower concentration. We have measured the dependency of these two peaks on the analyte concentration by calculating the I_{413}/I_{528} ratio and plotted it against the concentration of the analyte, as shown in Figure 5b. From this calibration curve, we deduced the limit of detection by taking the formula (3.3 × RSD)/slope and found to be 49.697 nM. The digital photographs of the sensing experiments in aqueous media are shown in Figure 5c. It is clear that on addition of TC to the nanoprobe solution, the fluorescence intensity goes on increasing, which changes the color of the solution from light blue to bright yellow green under UV light. Based on these findings, we have constructed a filter paper strip-based smartphone device capable of capturing images of TM-GO-SF QD-coated paper strips submerged in various TC concentrations. The color changes in the filter paper were properly monitored by the smartphone camera in the presence of 365 nm UV light (Figure 5d). A cylindrical shaped home-made mini-UV chamber (diameter, 4.4 cm; height, 7.5 cm) with an adjustable length was constructed for protection from outer influencing light that degrades the quality of the capturing images (Figure S2). It was attached in front of the rear camera of the mobile phone. A rectangular shaped discarded PCB of dimensions 1.5 cm × 1.5 cm was used for the installation of an electric circuit consisting of a 1 watt 365 nm LED (light-emitting diode, D1) powered from the battery of the mobile phone (output 5 V) with the help of an OTG cable and adaptor. A resistance of 10 ohms was connected in series so that a maximum current of 130 mA can pass through it (Figure 5f). The UV LEDs have emission peaks in the range 365−370 nm with a 120° viewing angle. The smartphone used for capturing the images basically consists of 108 megapixels.

A Samsung primary camera of maximum resolution (12,000 × 9000) with a pixel size 0.7 μm and focus f/1.9 is used. The schematic representation of the smart sensor including all accessories is demonstrated in Figure 5g. The captured images were visualized by a mobile phone application called "Color Grab" available in Google Play Store that is offered by lobomatix. The main function of this App is to analyze the red (R), green (G), and blue (B) color intensity of the captured images and convert them to readable numerical values. These data can be used to estimate the quantity of analytes present in the paper strip by plotting a calibration curve of R/G against the concentration of TC (Figure 5e). The detection limit for the smart sensing platform was found to be 0.125 μM in the linear range of 0.1−0.9 μM.

Optimization Conditions. The best possible conditions for the maximum emission of nanoprobes and their corresponding highest ability for the detection of TC in liquid phase were examined by changing several parameters, as discussed below. The pH of the sensing mixture usually affects the fluorescence intensity of the nanoprobe by changing the binding ability with the analytes. We have examined the possible effect of pH on the sensing performance of the present sensor system by monitoring the fluorescence intensity at different pH in both the absence and presence of TC and found that at pH = 8, the nanoprobe shows the maximum intensity in both the absence and presence of analytes in I_{413} and I_{528} regions, respectively (Figure S3a). Therefore, we choose pH 8 as the optimized condition for sensing. Additionally, in order to obtain the highest possible fluorescence intensity and an accurate RGB value, we adjusted the number of coating layers on the filter paper strip using TM-GO-SF QDs. To achieve this, we used grade 4 filter papers with pores between 20 and 25 μm, which are almost nonfluorescent in the presence of 365 nm UV light. We coated them with a TM-GO-SF QD solution by immersing the strip through forceps for 10 s and then drying in a vacuum oven for 10 min. The single-layer coated filter paper strip shows an R/G value of 0.572 in the presence of 0.2 μM TC. On further coating with the nanoprobe solution and treating with the same concentration of TC, the R/G value increases up to the third layer (R/G = 0.697) beyond which it decreases due to surface saturation. This effect is demonstrated in Figure S3b,c. Moreover, as shown in Figure S4, we also compared the fluorescence pictures from the custom-built UV chamber of our smart sensing platform with those from a standard UV chamber. Our system features a more efficient UV compartment with the benefits of mobility due to its small size and better influencing light cancellation.

Real Sample Analysis. We employed four different real samples in this study: fish samples, chicken samples, human blood serum, and honey samples. The collection and pretreatment of real sample solutions are discussed in the Supporting Information. This solution was mixed with PBS buffer (pH 7.4) where an adequate dose of TC was spiked. As

https://doi.org/10.1021/acsomega.3c01753
ACS Omega 2023, 8, 21914−21928

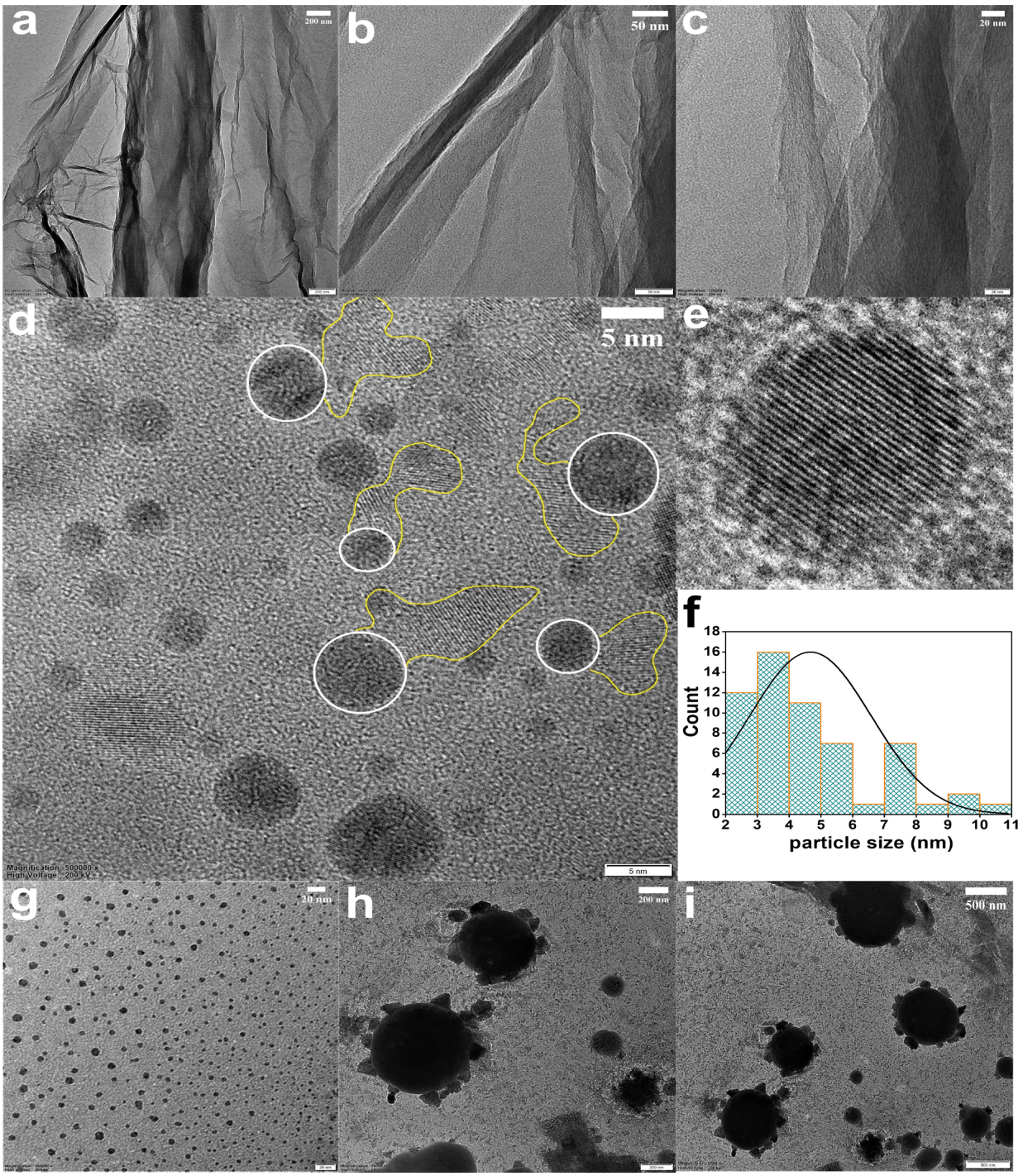

Figure 4. TEM images of a TM-GO sheet at 200 nm scale (a), 50 nm scale (b), and 20 nm scale (c). HRTEM images of TM-GO-SF QDs at 5 nm scale (d). Corresponding intermolecular distance between fringes (e) and the probability distribution of TM-GO-SF QDs at 5 nm scale (f). TM-GO-SF QDs at 20 nm scale (g) and the corresponding aggregated products in the presence of TC at 200 nm scale (h) and 500 nm scale (i).

indicated in Figure 6, the relevant fluorescence spectra were recorded. The detection limits for these ratiometric sensing emission spectra were computed using the same approach as for aqueous media, as described earlier. The detection limits were determined and found to be 47.76, 55.25, 47.90, and 45.78 nM for the chicken sample, fish sample, human blood serum, and honey sample, respectively, which are similar to the values evaluated from aqueous media, showing the sensor's reliability. Additionally, similar to the fluorescence spectrophotometric standard methods, we have tested the applicability of our smart sensing system by measuring the RGB color channel value of the filter paper strip immersed in the real sample media where a specific concentration of TC was spiked. The detailed process of the test sample preparation and the corresponding results are discussed in the Supporting Information. The accuracy of the methods was calculated by evaluating the recovery percentage, as shown in Table S1. The recovery % was found to be in the range of 97.84−100.09% with a relative standard deviation of 0.19−2.8%. This indicates

https://doi.org/10.1021/acsomega.3c01753
ACS Omega 2023, 8, 21914−21928

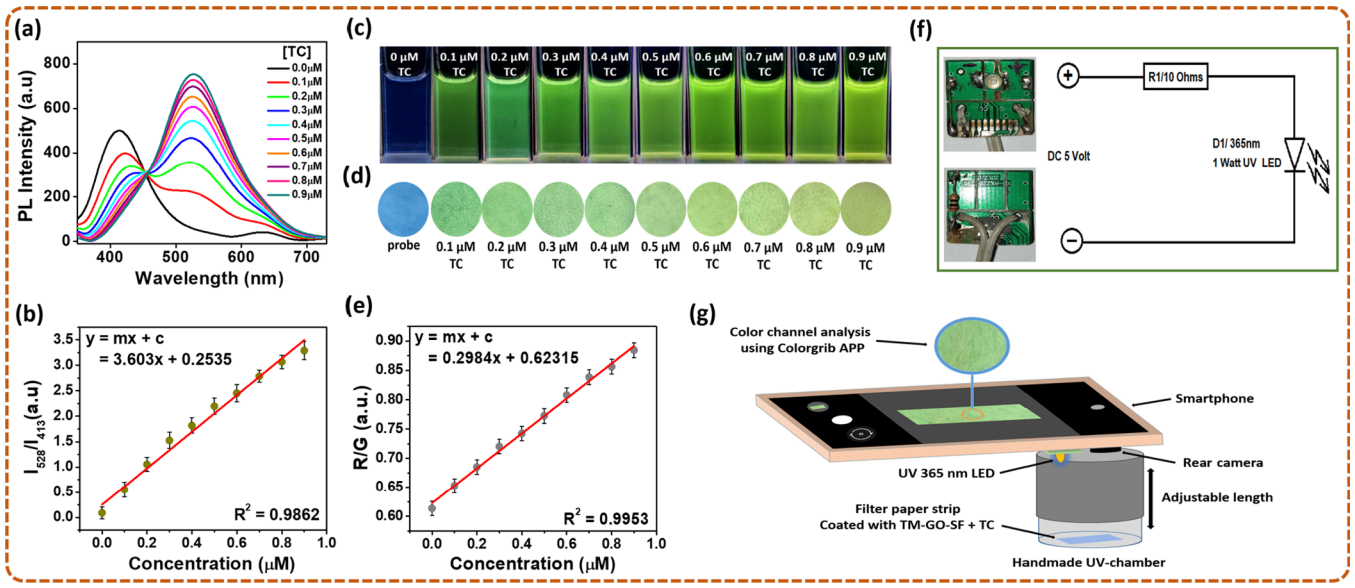

Figure 5. Photoluminescence spectra (a) and calibration plot (b) of ratiometric sensing of TC. Digital photograph of sensing in aqueous media (c) and filter paper strip-based sensing (d). Calibration plot for a smart sensing device (e), fabricated electrical circuit for an LED (f), and schematic diagram for a mobile-based smart sensing platform (g).

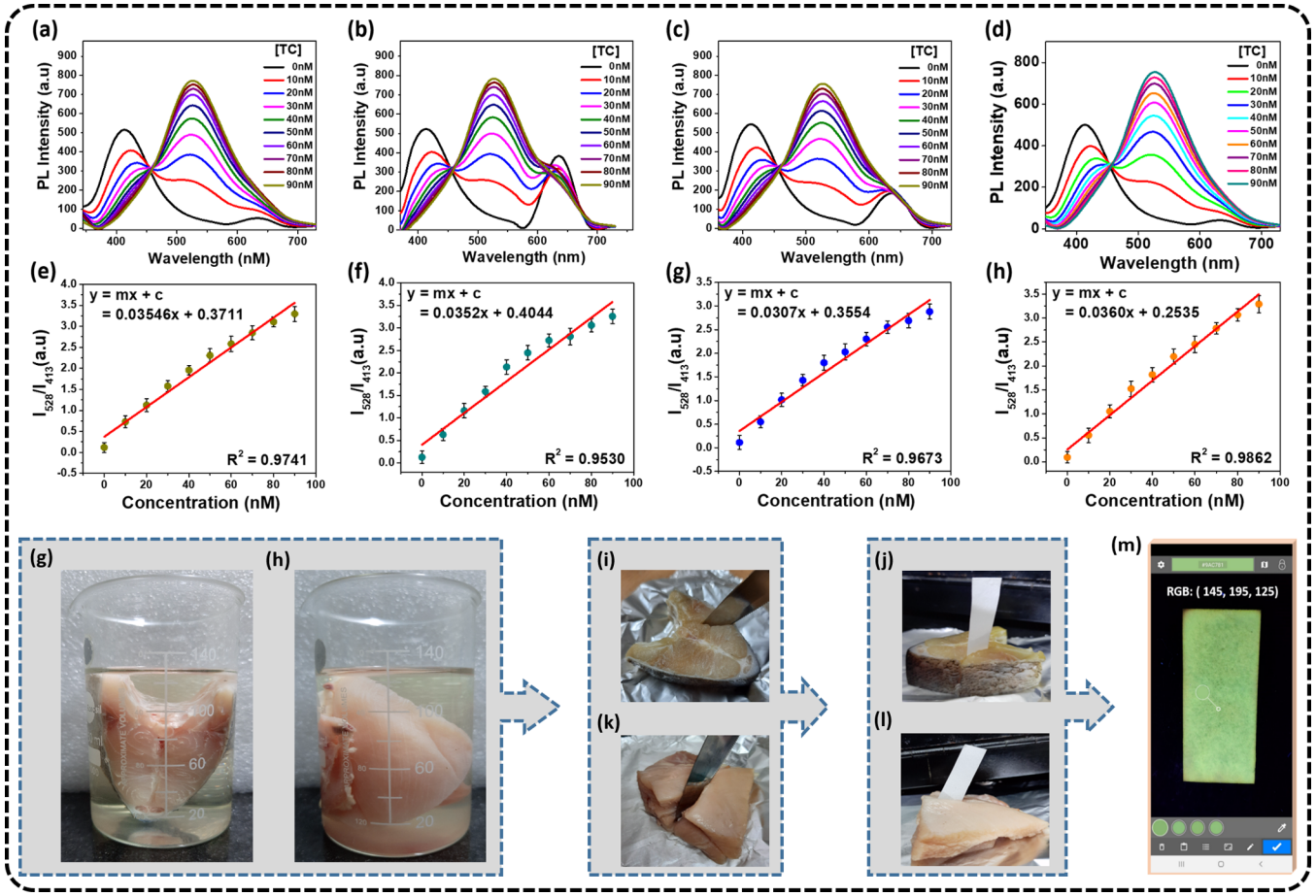

Figure 6. Fluorescent spectra of ratiometric fluorescence sensing of TC in biological samples (a), (b), (c), and (d) and their corresponding calibration plots (e), (f), (g), and (h) for human blood serum, honey sample, chicken sample, and fish sample, respectively. Digital images of the preparation of fish samples (g) and chicken samples (h); spiked TC and their edge cutting (i) and (k) for the insertion of the filter paper strip, (j) and (l) for fish and chicken samples, respectively. (m) Smartphone screenshot of a paper strip immersed in TC-spiked real samples (m).

the remarkable sensitivity and reliability of the sensor toward the detection of TC in real media.

Sensing Mechanism. By reviewing the existing literature, we looked into potential mechanisms for this ratiometric

https://doi.org/10.1021/acsomega.3c01753
ACS Omega 2023, 8, 21914−21928

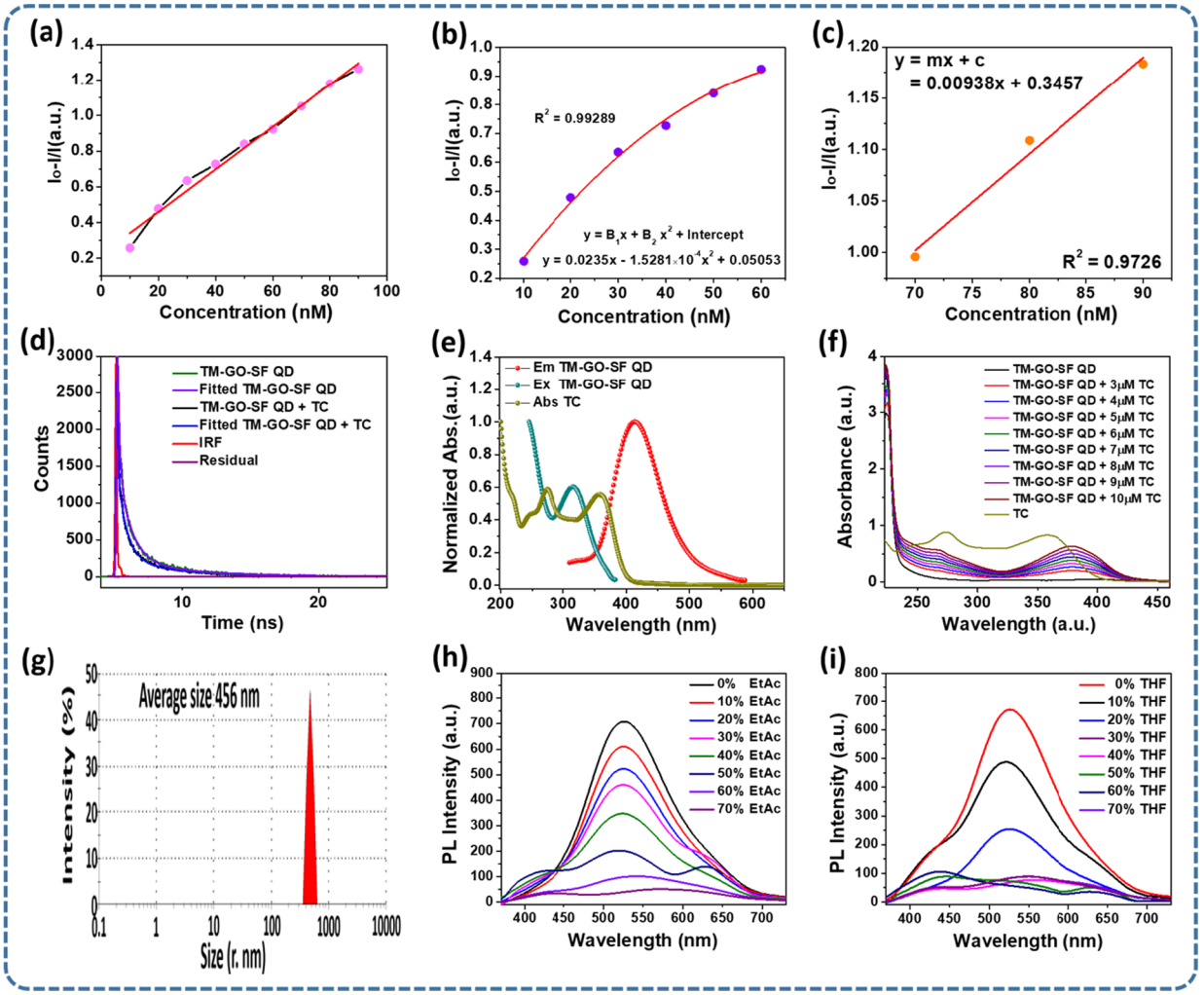

Figure 7. Stern–Volmer plot for ratiometric sensing of TC (a) and its polynomial (b) and linear fitting spectra (c). Time-resolved photoluminescent spectra (d), Overlap spectra for FRET (e), UV–vis spectra for ground-state complexation (f), and dynamic light-scattering spectra for the determination of particle size (g). Effect of solvent polarity in the aggregation process during ACQ for ethyl acetate (h) and tetrahydrofuran (i).

sensing process and discovered that most ratiometric sensors have a common quenching mechanism, such as FRET, IFE, PET, electrostatic interactions, and so forth. In our case also, the quenching effect at the (I_{413}) region can be inspected by evaluating the possible overlap between the absorption spectra of tetracycline and the emission or excitation spectra of the nanoprobe (Figure 7e). We found that the absorption spectra of TC overlap slightly the emission spectra of the nanoprobe, while a significant overlap was observed for the excitation spectra. This indicates that there is a possibility for either IFE or FRET to play a crucial role throughout the quenching process. Our analysis of the time-resolved fluorescence lifetime measurement experiment and calculation of the lifetime of the nanoprobe solution in the presence and absence of the TC content has been used to support this. We observed that the fluorescence lifetime of the nanoprobe changes from 1.12 to 0.32 ns with the addition of 30 nM concentration of TC. Such a decrease in lifetime value clearly indicates the involvement of the dynamic quenching process.[64] One such dynamic quenching mechanism is FRET, in which the sensor probe's lifetime changes as a result of its interactions with analytes. IFE, in contrast, is distinguished by the consistency in the lifetime value. Therefore, in our study, the sensor undergoes dynamic quenching pathways where FRET is the primary reason for this dynamic quenching of intensity. Sometimes, dynamic quenching lies parallel with a static quenching process where a combination of both these effects leads to a sufficient decrease in fluorescence intensity. To examine the existence of static quenching, we have measured the absorption spectra of the nanoprobe in the presence of an increasing concentration of TC, as shown in Figure 7f. In the presence of TC, the absorption spectra show characteristic new absorption maxima at two different regions, at 268 and 380 nm, which resemble the parent TC absorption spectra but only slightly red-shifted. This red shifting of the absorption maxima is a consequence of the appearance of a new emission peak at 528 nm whose intensity increases with the increasing concentration of TC. Such kind of variation in the absorption spectra is an indication of the formation of the ground-state complex between the excited-state nanoprobe and ground-state analyte, which is a feature of static quenching.[65] We further investigated the kinetics of TM-GO-SF QD interaction with TC by estimating the reaction rate at room temperature using the Langmuir–Hinshel–Wood (L–H) model.[66] For a pseudo-first-order reaction, the rate constant is calculated as follows

https://doi.org/10.1021/acsomega.3c01753
ACS Omega 2023, 8, 21914–21928

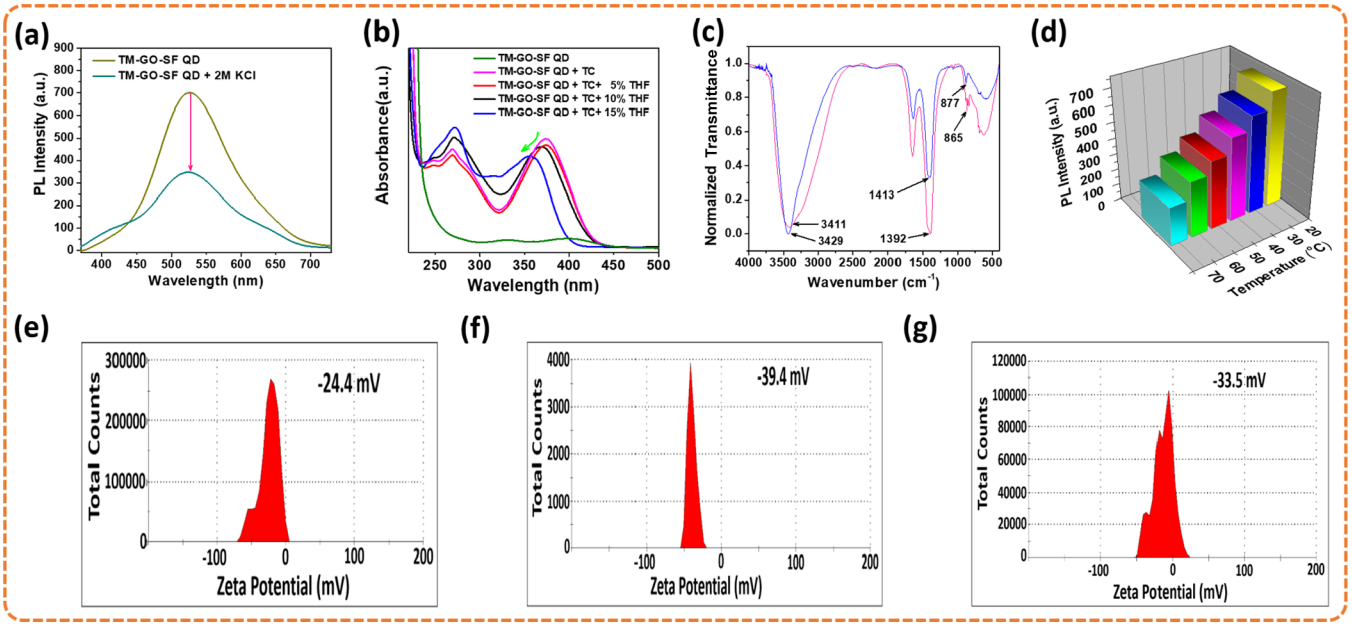

Figure 8. Fluorescence spectra for salt-screening effect (a), UV−vis absorption spectra of TM-GO-SF QDs in the presence of TC at different concentrations of THF (b), FT-IR spectra of the nanoprobe before and after the addition of TC (c), effect of temperature on the fluorescence intensity of the nanoprobe (d), surface zeta-potential spectra for TM-GO-SF QD + TC (e), TC (f), and TM-GO-SF QD (g).

$$\ln(C_t/C_o) = -k_1 t$$

where k_1 is the rate constant of the pseudo-first-order kinetics, and C_o and C_t are the concentrations at time zero and t, respectively. The plot of ln (C_t/C_o) versus t gives the change of reaction rate with respect to time, and its slope represents the rate constant k_1 (Figure S5). The detailed procedure for the determination of the reaction rate from the UV−vis spectra of the TM-GO-SF QDs + TC conjugate is discussed in the Supporting Information (Figure S5). Moreover, the extent of bonding between TM-GO-SF QDs and TC can be evaluated in terms of binding constant for this complexation using the Benesi−Hildebrandt relation.[67] When we express the Benesi−Hildebrandt relation in terms of fluorescence intensity, we get the following equation

$$\frac{1}{(I - I_o)} = \frac{1}{(I_1 - I_o)} + \frac{1}{(I_1 - I_o)K'[\mathrm{TC}]}$$

where I_o, I, and I_1 are the emission intensities of the nanoprobe in the absence of, at the intermediate state, and at the infinite concentration of TC, respectively. The plot of $\frac{1}{(I_1 - I_o)}$ versus $\frac{1}{[\mathrm{TC}]}$ gives a straight line (Figure S6), indicating the 1:1 complexation between TM-GO-SF QDs and TC, and the slope gives the binding constant K' for this complexation which is found to be 0.0525 M^{-1}. The value indicates that a strong binding interaction exists between the nanoprobe and TC.

All of the aforementioned data serve as a convincing evidence for the fact that both static and dynamic quenching are crucial to the quenching process. The correlation of these two quenching can be illustrated by evaluating the Stern Volmer plots as $I_o - I/I$ versus concentration of TC in DI water and other real media, as shown in Figures 7 and S7, respectively. We observed that, in every case, the S−V plot deviated from linearity from 10 to 50−60 nM concentration of TC, which is best fitted by the second-order polynomial equation, as shown below (Figures 7b and S7). This implies the coexistence of both dynamic and static quenching simultaneously. The corresponding equation is[65]

$$\frac{I_o}{I} = K_D K_S[Q]^2 + (K_D + K_S)[Q] + 1$$

In this polynomial equation, I and I_o represent the photoluminescence intensities in the presence and absence of TC, respectively. Q denotes the concentration of TC used, and K_D and K_S represent the quenching constants for dynamic and static quenching, respectively. The polynomial equations for both deionized water and real samples are mentioned in their respective plots. We further evaluate the dynamic quenching constant by rearranging the S−V plot for higher concentrations from 70 to 90 nM. We found that this did not significantly deviate from linearity for either real samples or deionized media, which supports the dynamic quenching at higher concentrations (Figures 7c and S7). The corresponding S−V equation for dynamic quenching is

$$\frac{I_o}{I} = 1 + K_D \cdot Q$$

The corresponding linear equations and R^2 values are shown in the respective plot. From the equation, the dynamic quenching constant can be evaluated and found to be 9.38 × 10^{-3} for deionized water. Similarly, to evaluate the static quenching constant, we have plotted $(I_o/I - 1)/[Q]$ against the concentration of TC according to the following equation[65]

$$\frac{I_o}{I} - 1/[Q] = K_D K_S[Q] + (K_D + K_S)$$

where $K_D K_S$ and $K_D + K_S$ are the slopes and intercepts of the graph (Figure S8). The solution of the above quadratic equation is

$$K_S^2 + 0.227K_S - 0.301$$

https://doi.org/10.1021/acsomega.3c01753
ACS Omega 2023, 8, 21914−21928

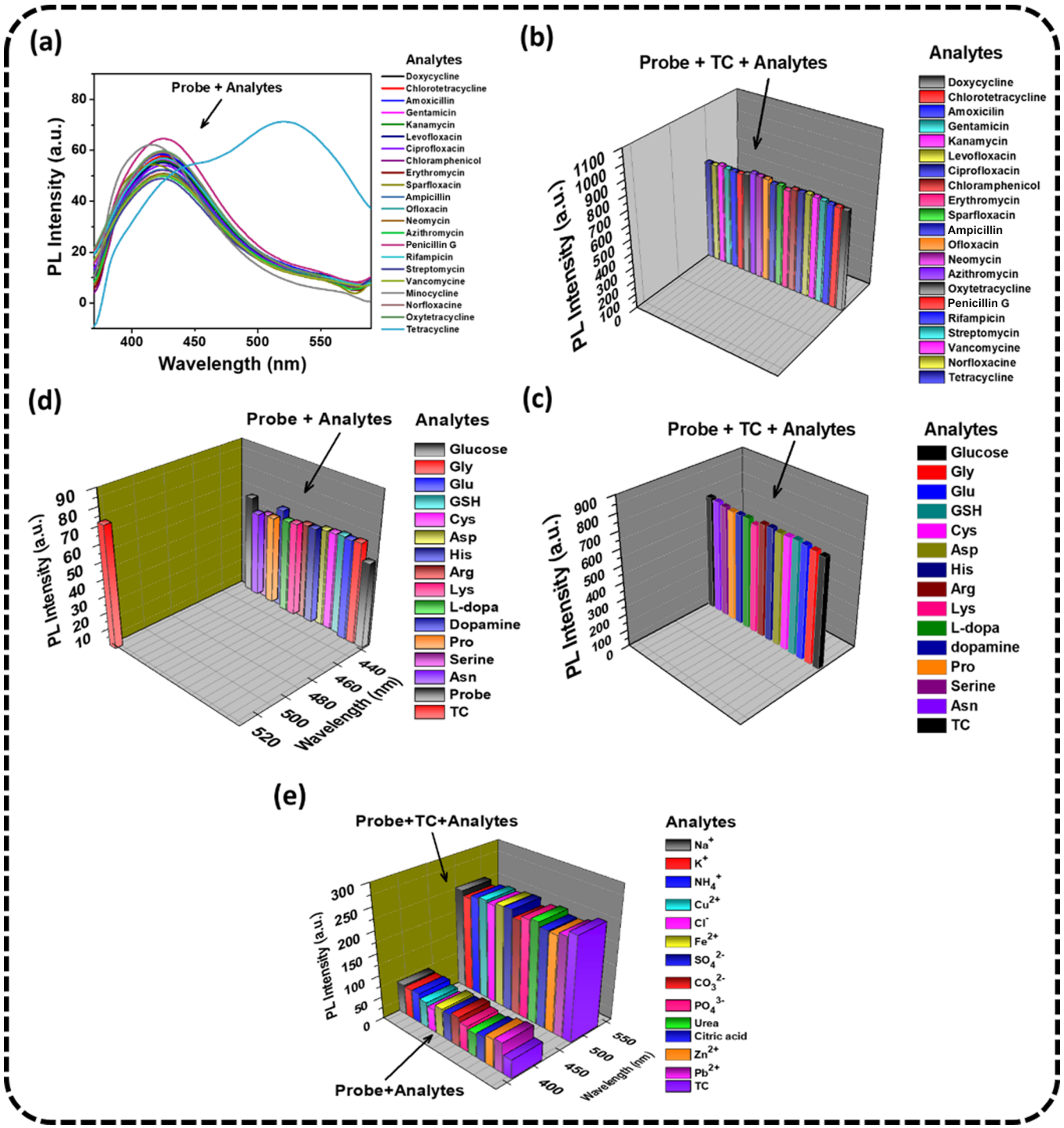

Figure 9. Fluorescence spectra of TM-GO-SF QDs in the presence of different antibiotics (a) and their interference effect in the presence of TC (b). Interference of different amino acids (c) and their selectivity in the presence of TC (d). Selectivity test of the nanoprobe using different ions and interfering molecules (e).

We can calculate the values of K_S from this equation to be 0.6741 or 0.4471 (Figure S8). Since the dynamic quenching constant has the value 9.38×10^{-3}, the higher value 0.6741 is assigned to the static quenching constant.

We have examined the possible structural changes that occur during the Meisenheimer complex formation process with the help of TEM and found that a spherical aggregated molecular structure of average diameter 481.59 nm is formed when TM-GO-SF QDs interact with TC, as shown in Figure 4g,h. The aggregated process was further confirmed with the DLS study where a sufficient increment in the size (456 nm) of the QD materials was observed after interaction with TC molecules (Figure 7g). Furthermore, we have confirmed the aggregation possibility in aqueous media by changing the polarity of the solvents, as shown in Figure 7h,i. In the presence of a nonpolar solvent, the fluorescent emission spectra of the nanoprobe diminished significantly which clearly indicates that the aggregation-caused quenching (ACQ) effect also plays a significant role during the quenching process.[68] To confirm further the aggregation process, we have recorded the emission

https://doi.org/10.1021/acsomega.3c01753
ACS Omega 2023, 8, 21914−21928

spectrum of TM-GO-SF QDs with 90 nM TC in a highly saturated salt solution of 2 M KCl (Figure 8a). We observed that there is a sufficient drop of fluorescence intensity of the nanoprobe that can be explained by considering the salt-screening effect. In a highly saturated salt solution, the nanoprobe and analyte molecules are surrounded by the constituent oppositely charged ionic components of the salt which hinder them to approach in close vicinity to each other and prohibit the aggregation.[69] For this reason, there is a sufficient drop of the emission intensity, as observed clearly from Figure 8a. This phenomenon inversely supports the existence of aggregation which causes fluorescence quenching. Aggregation-caused quenching (ACQ) effect mainly arises when the molecules with delocalized structures experience strong $\pi-\pi$ stacking when they approach in close proximity to each other and get aggregated. In the aggregated state, both the donor and acceptor moieties transfer energy which is subsequently consumed by the activation of nonradiative pathways, and therefore the fluorescence intensity decreases. This effect is favored by several bonding and nonbonding interactions between donor and acceptor complexes such as hydrogen-bonding and electrostatic interactions, which alternately promoted $\pi-\pi$ stacking via the formation of aggregates.[32,68] To establish the ACQ effect, we have examined the change in the absorption spectra of TM-GO-SF QDs in the presence of TC at increasing concentrations of the low-polarity solvent THF (Figure 8b). On increasing the THF content, the absorption spectra decrease gradually up to a limit, beyond which it shifted instantly from 375 to 356.5 nm. This blue shift of absorption spectra toward the lower wavelength can be attributed to the decrease of $\pi-\pi$ stacking interaction due to the tendency of the aggregated product to fall apart due to the lower polarity of the solvent. This sensitivity effect of the nanoprobe toward the change of polarity of the solvent in the presence of TC strongly supported the existence of $\pi-\pi$ stacking interaction in the aggregated form of the sensor which ultimately provides a strong evidence for fluorescence quenching through the ACQ effect.[70] The possible interaction between the nanoprobe and TC is further analyzed by FT-IR spectra and zeta-potential experiments, as shown in Figure 8. In the presence of TC, the O−H stretching frequency of the TM-GO-SF QDs decreases from 3429 to 3411 cm^{-1}, while the N−H stretching frequency changes from 1413 to 1392 cm^{-1}, as shown in Figure 8c. These significant changes in O−H and N−H stretching vibrations clearly indicate that hydrogen bonding plays a significant role in the binding process between the transducer and analyte moieties.[69] The zeta-potential value before and after interaction with TC (−39.4 mV), as shown in Figure 8e−g, which changes from −33.5 to −24.4 mV, respectively, indicates that the electrostatic interaction is the reason for aggregation.[71,72] Temperature also has a significant influence on the ACQ effect. At a higher temperature, the aggregated molecules acquire energy that is utilized to increase the intermolecular motion which decreases the nonbonding interaction between the aggregated donor-acceptor moieties. As a results, there is a gradual drop of fluorescence intensity with the increasing temperature of the sensing media.[73] The results are shown in Figure 8d.

Thus, in summary, it can be concluded that the above ratiometric sensing involves both static and dynamic quenching along with the ACQ effect, where the formation of ground-state complexation occurs, which is assigned to a newly appearing absorption peak on a longer wavelength region. The intensity of this peak increases gradually with respect to the concentration of TC. The corresponding emission spectra of this TM-GO-SF QD + TC conjugate exhibit a successive increase in fluorescence intensity at the (I_{528}) region.

Interference Study. We further looked at how possible bioactive substances with similar structural features can interfere and change the emission characteristics of the TM-GO-SF QD, as shown in Figure 9. For this purpose, we recorded the emission spectra of the nanoprobe with the addition of different antibiotics, amino acids, and common biomolecules, as shown in Figure 9, with the analyte concentration of 30 nM each. All of these instances show that TC binds preferentially with the nanoprobe in the presence of other interfering molecules, which is clearly distinguished by the emission maxima moving from 413 to 528 nm. However, other analytes do not exhibit this behavior, indicating that there is no interference from them. Moreover, various ions and solvents may also affect selectivity when sensing is done in an aqueous solution by generating ionic complexes with analytes or nanoprobes. Because of this, we investigated the selectivity test in the presence of ions and lab solvents and found that they have no impact on the selective binding of TC in an aqueous environment (Figure 9e). The aforementioned results show that the sensor is very selective and has excellent TC detection accuracy. Such an optical sensor has great promise for application scenarios using real samples and might be used to identify environmental pollutants.

Comparative Study. A review of the literature was conducted to determine whether the suggested sensor system had a higher sensing efficiency when compared to other sensor systems that were already in use. Details are provided in the Supporting Information (SI).

CONCLUSIONS

In this study, thiol-ene click chemistry was used to synthesize novel zero-dimensional quantum dot materials possessing characteristic fluorescence properties. This nanoprobe material selectively binds TC present in aqueous real samples through hydrogen bonding and electrostatic interaction to form an aggregated product, as confirmed by the TEM, FT-IR, and zeta-potential data. This combined product demonstrates distinctive fluorescence emission properties, wherein the quenching of the intensity of the parent emission peak synergistically increases the intensity of the newly generated shoulder peak through a ratio that depends on the concentration of TC. This newly formed peak is a consequence of complexation that occurs between the sensor and analyte which shows a gradual shifting of color in aqueous media under UV light of 365 nm. This behavior inspires us to fabricate a paper strip-based portable smart sensor using the smartphone color channel readout technology which can detect the TC residue in aqueous media with an LOD of 0.125 μM. Compared to the other reported methods, our sensor system possesses high selectivity in the presence of other interfering biological moieties and is built around a cost-effective material. The practical applicability of this sensor system was tested in real samples, viz., chicken sample, fish sample, human blood serum, and honey sample, with the detection limits of 47.7634, 55.253, 47.9030, and 45.784 nM, respectively, on the linear ranges of 0−90 Nm. This type of sensor can also be used for the immediate identification of

https://doi.org/10.1021/acsomega.3c01753
ACS Omega 2023, 8, 21914−21928

dangerous foodborne pathogens and other adulterations that pose a substantial risk to consumer health.

■ ASSOCIATED CONTENT

Supporting Information

The Supporting Information is available free of charge at https://pubs.acs.org/doi/10.1021/acsomega.3c01753.

Photoluminescence properties of TM-GO-SF-QDs, prototype device fabrication details, optimized fluorescence sensing conditions, pretreatment procedure and analysis results of the real samples, kinetic studies, Stern−Volmer's plot for ratiometric sensing in real samples, and comparative studies (PDF)

■ AUTHOR INFORMATION

Corresponding Author

Neelotpal Sen Sarma − *Advanced Materials Laboratory, Institute of Advanced Study in Science and Technology, Guwahati 781035 Assam, India; Academy of Scientific and Innovative Research (AcSIR), Ghaziabad 201002, India;* orcid.org/0000-0002-2666-6316; Phone: +91(0361) 2270084; Email: neelot@iasst.gov.in; Fax: (0361) 2740659

Author

Kangkan Jyoti Goswami − *Advanced Materials Laboratory, Institute of Advanced Study in Science and Technology, Guwahati 781035 Assam, India; Academy of Scientific and Innovative Research (AcSIR), Ghaziabad 201002, India*

Complete contact information is available at: https://pubs.acs.org/10.1021/acsomega.3c01753

Author Contributions

All authors have given approval to the final version of the manuscript.

Notes

The authors declare no competing financial interest.

■ ACKNOWLEDGMENTS

K.J.G. and N.S.S. acknowledge DST, Government of India, for the financial support through the Institute of Advanced Study in Science and Technology (IASST). The authors thank Sophisticated Analytical Instrumentation Centre (SAIC), IASST, for providing the instrumental facilities.

■ REFERENCES

(1) Tian, P.; Tang, L.; Teng, K.; Lau, S. P. Graphene quantum dots from chemistry to applications. *Mater. Today Chem.* **2018**, *10*, 221−258.

(2) Ji, C.; Zhou, Y.; Leblanc, R. M.; Peng, Z. Recent developments of carbon dots in biosensing: A review. *ACS Sensors* **2020**, *5*, 2724−2741.

(3) Chen, H.; Gao, Q.; Li, J.; Lin, J. M. Graphene materials-based chemiluminescence for sensing. *J. Photochem. Photobiol.* **2016**, *27*, 54−71.

(4) Zheng, X. T.; Ananthanarayanan, A.; Luo, K. Q.; Chen, P. Glowing graphene quantum dots and carbon dots: properties, syntheses, and biological applications. *Small* **2015**, *11*, 1620−1636.

(5) Zeng, R.; Luo, Z.; Zhang, L.; Tang, D. Platinum nanozyme-catalyzed gas generation for pressure-based bioassay using polyaniline nanowires-functionalized graphene oxide framework. *Anal. Chem.* **2018**, *90*, 12299−12306.

(6) Shu, J.; Qiu, Z.; Tang, D. Self-referenced smartphone imaging for visual screening of H2S using Cu x O-polypyrrole conductive aerogel doped with graphene oxide framework. *Anal. Chem.* **2018**, *90*, 9691−9694.

(7) Zhou, Q.; Lin, Y.; Zhang, K.; Li, M.; Tang, D. Reduced graphene oxide/BiFeO3 nanohybrids-based signal-on photoelectrochemical sensing system for prostate-specific antigen detection coupling with magnetic microfluidic device. *Biosens. Bioelectron.* **2018**, *101*, 146−152.

(8) Li, M.; Chen, T.; Gooding, J. J.; Liu, J. Review of carbon and graphene quantum dots for sensing. *ACS Sens.* **2019**, *4*, 1732−1748.

(9) Zhang, Y.; Lv, M.; Gao, P.; Zhang, G.; Shi, L.; Yuan, M.; Shuang, S. The synthesis of high bright silver nanoclusters with aggregation-induced emission for detection of tetracycline. *Sens. Actuators B Chem.* **2021**, *326*, No. 129009.

(10) Yuan; An, J.; Zhang, G.; Hu, Y.; Luo, M.; Shi, Y.; Liu, Y. In-situ nitrogen-doped carbon dots for fluorescence sensing of tetracycline antibiotic. *Ceram. Int.* **2022**, *48*, 4047−4054.

(11) Sun, P.; Yang, D.; Li, J.; Zhang, Y. Aggregation-induced emission of 4-formyl-3-hydroxybenzoic acid for the ratiometric fluorescence detection of tetracycline antibiotics. *Dyes Pigm.* **2022**, *197*, No. 109841.

(12) Zhao, Y.; Wang, Q.; Wang, H.; Zhangsun, H.; Sun, X.; Bu, T.; Liu, Y.; Wang, W.; Xu, Z.; Wang, L. Europium-based metal-organic framework containing characteristic metal chains: a novel turn-on fluorescence sensor for simultaneous high-performance detection and removal of tetracycline. *Sens. Actuators B Chem.* **2021**, *334*, No. 129610.

(13) Hu, X.; Zhao, Y.; Dong, J.; Liu, C.; Qi, Y.; Fang, G.; Wang, S. A strong blue fluorescent nanoprobe based on Mg/N co-doped carbon dots coupled with molecularly imprinted polymer for ultrasensitive and highly selective detection of tetracycline in animal-derived foods. *Sens. Actuators B Chem.* **2021**, *338*, No. 129809.

(14) Taghdisi, S. M.; Danesh, N. M.; Ramezani, M.; Abnous, K. A novel M-shape electrochemical aptasensor for ultrasensitive detection of tetracyclines. *Biosens. Bioelctron.* **2016**, *85*, 509−514.

(15) Wang, H.-H.; Zhang, Y.; Yang, D.-B.; Hou, L.; Li, Z.-Y.; Wang, Y. Y. Fluorine-substituted regulation in two comparable isostructural Cd (II) coordination polymers: enhanced fluorescence detection for tetracyclines in water. *Cryst. Growth Des.* **2021**, *21*, 2488−2497.

(16) Bougrini, M.; Florea, A.; Cristea, C.; Sandulescu, R.; Vocanson, F.; Errachid, A.; Bouchikhi, B.; El Bari, N.; Jaffrezic-Renault, N. Development of a novel sensitive molecularly imprinted polymer sensor based on electropolymerization of a microporous-metal-organic framework for tetracycline detection in honey. *Food Control.* **2016**, *59*, 424−429.

(17) Sri, S.; Singh, U.; Kumar, R.; Lakshmi, G.; Solanki, P. R. Ignition of photoluminescent intensity of quenched MoS2 quantum dots tetracycline mixture by levofloxacin via photoinduced electron transfer. *JCIS Open.* **2021**, *3*, No. 100021.

(18) Li, C.; Zeng, C.; Chen, Z.; Jiang, Y.; Yao, H.; Yang, Y.; Wong, W. T. Luminescent lanthanide metal-organic framework test strip for immediate detection of tetracycline antibiotics in water. *J. Hazard. Mater.* **2020**, *384*, No. 121498.

(19) Hou, J.; Li, H.; Wang, L.; Zhang, P.; Zhou, T.; Ding, H.; Ding, L. Rapid microwave-assisted synthesis of molecularly imprinted polymers on carbon quantum dots for fluorescent sensing of tetracycline in milk. *Talanta* **2016**, *146*, 34−40.

(20) Gissawong, N.; Boonchiangma, S.; Mukdasai, S.; Srijaranai, S. Vesicular supramolecular solvent-based microextraction followed by high performance liquid chromatographic analysis of tetracyclines. *Talanta* **2019**, *200*, 203−211.

(21) Wang, T.; Mei, Q.; Tao, Z.; Wu, H.; Zhao, M.; Wang, S.; Liu, Y. A smartphone-integrated ratiometric fluorescence sensing platform for visual and quantitative point-of-care testing of tetracycline. *Biosens. Bioelctron.* **2020**, *148*, No. 111791.

(22) Zhou, X.; Xing, D.; Zhu, D.; Tang, Y.; Jia, L. Development and application of a capillary electrophoresis−electrochemiluminescent

method for the analysis of enrofloxacin and its metabolite ciprofloxacin in milk. *Talanta* **2008**, *75*, 1300−1306.
(23) Ji, H.; Xia, C.; Xu, J.; Wu, X.; Qiao, L.; Zhang, C. A highly sensitive immunoassay of pesticide and veterinary drug residues in food by tandem conjugation of bi-functional mesoporous silica nanospheres. *Analyst* **2020**, *145*, 2226−2232.
(24) Ma, X.; Pang, C.; Li, S.; Xiong, Y.; Li, J.; Luo, J.; Yang, Y. Synthesis of Zr-coordinated amide porphyrin-based two-dimensional covalent organic framework at liquid-liquid interface for electrochemical sensing of tetracycline. *Biosens. Bioelectron.* **2019**, *146*, No. 111734.
(25) Wang, Q.; Liu, Y.; Bai, Y.; Yao, S.; Wei, Z.; Zhang, M.; Wang, L.; Wang, L. Superhydrophobic SERS substrates based on silver dendrite-decorated filter paper for trace detection of nitenpyram. *Anal. Chim. Acta* **2019**, *1049*, 170−178.
(26) Wang, L.; Su, D.; Berry, S. N.; Lee, J.; Chang, Y. T. A new approach for turn-on fluorescence sensing of l-DOPA. *Chem. Commun.* **2017**, *53*, 12465−12468.
(27) Yin, H.-Q.; Yang, J.-C.; Yin, X.-B. Ratiometric fluorescence sensing and real-time detection of water in organic solvents with one-pot synthesis of Ru@ MIL-101 (Al)−NH2. *Anal. Chem.* **2017**, *89*, 13434−13440.
(28) Han, J.; Zou, H. Y.; Gao, M. X.; Huang, C. Z. A graphitic carbon nitride based fluorescence resonance energy transfer detection of riboflavin. *Talanta* **2016**, *148*, 279−284.
(29) Zhu, J.; Chu, H.; Shen, J.; Wang, C.; Wei, Y. Green preparation of carbon dots from plum as a ratiometric fluorescent probe for detection of doxorubicin. *Opt. Mater.* **2021**, *114*, No. 110941.
(30) Xu, N.; Yuan, Y.; Yin, J.-H.; Wang, X.; Meng, L. One-pot hydrothermal synthesis of luminescent silicon-based nanoparticles for highly specific detection of oxytetracycline via ratiometric fluorescent strategy. *RSC Adv.* **2017**, *7*, 48429−48436.
(31) Cao, Y.; Wang, X.; Bai, H.; Jia, P.; Zhao, Y.; Liu, Y.; Wang, L.; Zhuang, Y.; Yue, T. Fluorescent detection of tetracycline in foods based on carbon dots derived from natural red beet pigment. *LWT* **2022**, *157*, No. 113100.
(32) Mei, J.; Leung, N. L.; Kwok, R. T.; Lam, J. W.; Tang, B. Z. Aggregation-induced emission: together we shine, united we soar! *Chem. Rev.* **2015**, *115*, 11718−11940.
(33) Ma, X.; Sun, R.; Cheng, J.; Liu, J.; Gou, F.; Xiang, H.; Zhou, X. Fluorescence aggregation-caused quenching versus aggregation-induced emission: a visual teaching technology for undergraduate chemistry students. *J. Chem. Educ.* **2016**, *93*, 345−350.
(34) Zeng, R.; Qiu, M.; Wan, Q.; Huang, Z.; Liu, X.; Tang, D.; Knopp, D. Smartphone-based electrochemical immunoassay for point-of-care detection of SARS-CoV-2 nucleocapsid protein. *Anal. Chem.* **2022**, *94*, 15155−15161.
(35) Cai, G.; Yu, Z.; Tong, P.; Tang, D. Ti 3 C 2 MXene quantum dot-encapsulated liposomes for photothermal immunoassays using a portable near-infrared imaging camera on a smartphone. *Nanoscale* **2019**, *11*, 15659−15667.
(36) Kitchawengkul, N.; Prakobkij, A.; Anutrasakda, W.; Yodsin, N.; Jungsuttiwong, S.; Chunta, S.; Amatatongchai, M.; Jarujamrus, P. Mimicking peroxidase-like activity of nitrogen-doped carbon dots (N-CDs) coupled with a laminated three-dimensional microfluidic paper-based analytical device (laminated 3D-μPAD) for smart sensing of total cholesterol from whole blood. *Anal. Chem.* **2021**, *93*, 6989−6999.
(37) Delaney, J. L.; Hogan, C. F.; Tian, J.; Shen, W. Electrogenerated chemiluminescence detection in paper-based microfluidic sensors. *Anal. Chem.* **2011**, *83*, 1300−1306.
(38) Li, L.; Huang, X.; Liu, W.; Shen, W. Control performance of paper-based blood analysis devices through paper structure design. *ACS Appl. Mater. Interfaces* **2014**, *6*, 21624−21631.
(39) Fu, Q.; Zhang, C.; Xie, J.; Li, Z.; Qu, L.; Cai, X.; Ouyang, H.; Song, Y.; Du, D.; Lin, Y. Ambient light sensor based colorimetric dipstick reader for rapid monitoring organophosphate pesticides on a smart phone. *Anal. Chim. Acta* **2019**, *1092*, 126−131.
(40) Zhao, J.; Chen, Y.; Du, P.; Li, J.; Zhang, Z.; Lu, X. Portable smartphone platform integrated with fluorescent test strip based on Eu3+−functionalized copper nanoclusters for on-site visual recognition of a pathogenic biomarker. *Sens. Actuators B Chem.* **2021**, *332*, No. 129495.
(41) Wang, H.; Da, L.; Yang, L.; Chu, S.; Yang, F.; Yu, S.; Jiang, C. Colorimetric fluorescent paper strip with smartphone platform for quantitative detection of cadmium ions in real samples. *J. Hazard. Mater.* **2020**, *392*, No. 122506.
(42) Yu, Z.; Gong, H.; Xue, F.; Zeng, Y.; Liu, X.; Tang, D. Flexible and high-throughput photothermal biosensors for rapid screening of acute myocardial infarction using thermochromic paper-based image analysis. *Anal. Chem.* **2022**, *94*, 13233−13242.
(43) Lv, S.; Tang, Y.; Zhang, K.; Tang, D. Wet NH3-triggered NH2-MIL-125 (Ti) structural switch for visible fluorescence immunoassay impregnated on paper. *Anal. Chem.* **2018**, *90*, 14121−14125.
(44) Qiu, Z.; Shu, J.; Tang, D. Bioresponsive release system for visual fluorescence detection of carcinoembryonic antigen from mesoporous silica nanocontainers mediated optical color on quantum dot-enzyme-impregnated paper. *Anal. Chem.* **2017**, *89*, 5152−5160.
(45) Maddinedi, S. B.; Mandal, B. K.; Vankayala, R.; Kalluru, P.; Pamanji, S. R.; Spectroscopy, B. Bioinspired reduced graphene oxide nanosheets using Terminalia chebula seeds extract. *Spectrochim. Acta A* **2015**, *145*, 117−124.
(46) Luong, N. D.; Sinh, L. H.; Johansson, L. S.; Campell, J.; Seppälä, J. Functional Graphene by Thiol-ene Click Chemistry. *Eur. J. Chem.* **2015**, *21*, 3183−3186.
(47) Liu, J.; Yuan, W.; Li, C.; Cheng, M.; Su, Y.; Xu, L.; Chu, T.; Hou, S. l-Cysteine-Modified Graphene Oxide-Based Membrane for Chiral Selective Separation. *ACS Appl. Mater. Interfaces* **2021**, *13*, 49215−49223.
(48) Eivazzadeh-Keihan, R.; Radinekiyan, F.; Madanchi, H.; Aliabadi, H. A. M.; Maleki, A. Graphene oxide/alginate/silk fibroin composite as a novel bionanostructure with improved blood compatibility, less toxicity and enhanced mechanical properties. *Carbohyr. Polym.* **2020**, *248*, No. 116802.
(49) Zhang, J.; Yang, H.; Shen, G.; Cheng, P.; Zhang, J.; Guo, S. Reduction of graphene oxide via L-ascorbic acid. *Chem. Commun.* **2010**, *46*, 1112−1114.
(50) Li, D.; Müller, M. B.; Gilje, S.; Kaner, R. B.; Wallace, G. G. Processable aqueous dispersions of graphene nanosheets. *Nat. Nanotechnol.* **2008**, *3*, 101−105.
(51) Monajati, M.; Borandeh, S.; Hesami, A.; Mansouri, D.; Tamaddon, A. M. Immobilization of L-asparaginase on aspartic acid functionalized graphene oxide nanosheet: enzyme kinetics and stability studies. *Chem. Eng. J.* **2018**, *354*, 1153−1163.
(52) Abdolhosseinzadeh, S.; Asgharzadeh, H.; Seop Kim, H. Fast and fully-scalable synthesis of reduced graphene oxide. *Sci. Rep.* **2015**, *5*, 10160.
(53) Zhang, C.; Zhang, Y.; Shao, H.; Hu, X. Hybrid silk fibers dry-spun from regenerated silk fibroin/graphene oxide aqueous solutions. *ACS Appl. Mater. Interfaces* **2016**, *8*, 3349−3358.
(54) Gong, D.; Yin, Y.; Chen, H.; Guo, B.; Wu, P.; Wang, Y.; Yang, Y.; Li, Z.; He, Y.; Zeng, G. Interfacial ions sieving for ultrafast and complete desalination through 2D nanochannel defined graphene composite membranes. *ACS Nano* **2021**, *15*, 9871−9881.
(55) Moon, I. K.; Lee, J.; Ruoff, R. S.; Lee, H. Reduced graphene oxide by chemical graphitization. *Nat. Commun.* **2010**, *1*, 73.
(56) Wang, Y.; Shi, Z.; Yin, J. Facile synthesis of soluble graphene via a green reduction of graphene oxide in tea solution and its biocomposites. *ACS Appl. Mater. Interfaces* **2011**, *3*, 1127−1133.
(57) Yang, A.; Li, J.; Zhang, C.; Zhang, W.; Ma, N. One-step amine modification of graphene oxide to get a green trifunctional metal-free catalyst. *Appl. Surf. Sci.* **2015**, *346*, 443−450.
(58) Marrani, A. G.; Zanoni, R.; Schrebler, R.; Dalchiele, E. A. Toward graphene/silicon interface via controlled electrochemical reduction of graphene oxide. *J. Phys. Chem. C* **2017**, *121*, 5675−5683.
(59) Sapner, V. S.; Chavan, P. P.; Sathe, B. R. L-Lysine-functionalized reduced graphene oxide as a highly efficient electro-

https://doi.org/10.1021/acsomega.3c01753
ACS Omega 2023, 8, 21914−21928

catalyst for enhanced oxygen evolution reaction. *ACS Sustainable Chem. Eng.* **2020**, *8*, 5524−5533.
(60) Zhao, G.; Qing, H.; Huang, G.; Genin, G. M.; Lu, T. J.; Luo, Z.; Xu, F.; Zhang, X. Reduced graphene oxide functionalized nanofibrous silk fibroin matrices for engineering excitable tissues. *NGP Asia Mater.* **2018**, *10*, 982−994.
(61) Nilogal, P.; Uppine, G. B.; Rayaraddi, R.; Sanjeevappa, H. K.; Martis, L. J.; Narayana, B.; Yallappa, S. Conductive in situ reduced graphene oxide−silk fibroin bionanocomposites. *ACS Omega* **2021**, *6*, 12995−13007.
(62) Pandit, S.; De, M. Interaction of amino acids and graphene oxide: trends in thermodynamic properties. *J. Phys. Chem. C* **2017**, *121*, 600−608.
(63) Piñeiro-García, A.; Vega-Díaz, S. M.; Tristán, F.; Meneses-Rodríguez, D.; Labrada-Delgado, G. J.; Semetey, V. New insights in the chemical functionalization of graphene oxide by thiol-ene Michael addition reaction. *FlatChem.* **2021**, *26*, No. 100230.
(64) Kumar, V.; Maiti, B.; Chini, M. K.; De, P.; Satapathi, S. Multimodal fluorescent polymer sensor for highly sensitive detection of nitroaromatics. *Sci. Rep.* **2019**, *9*, 7269.
(65) Tanwar, A. S.; Parui, R.; Garai, R.; Chanu, M. A.; Iyer, P. K. Dual "Static and Dynamic" fluorescence quenching mechanisms based detection of TNT via a cationic conjugated polymer. *ACS Meas. Sci. Au.* **2022**, *2*, 23−30.
(66) Borah, D.; Saikia, P.; Sarmah, P.; Gogoi, D.; Das, A.; Rout, J.; Bhattacharjee, C. R. Photocatalytic and Antibacterial Activity of Fluorescent CdS Quantum Dots Synthesized Using Aqueous Extract of Cyanobacterium Nostoc carneum. *BioNanoSci* **2023**, *13*, 650−666.
(67) Singh, R. B.; Mahanta, S.; Bagchi, A.; Guchhait, N. Interaction of human serum albumin with charge transfer probe ethyl ester of N, N-dimethylamino naphthyl acrylic acid: An extrinsic fluorescence probe for studying protein micro-environment. *Photochem. Photobiol. Sci.* **2009**, *8*, 101−110.
(68) Yang, H.; Liu, Y.; Guo, Z.; Lei, B.; Zhuang, J.; Zhang, X.; Liu, C.; Hu, C. Hydrophobic carbon dots with blue dispersed emission and red aggregation-induced emission. *Nat. Commun.* **2019**, *10*, 1789.
(69) Gogoi, B.; Sen Sarma, N. Curcumin−cysteine and curcumin−tryptophan conjugate as fluorescence turn on sensors for picric acid in aqueous media. *ACS Appl. Mater. Interfaces* **2015**, *7*, 11195−11202.
(70) Park, M.; Jeong, Y.; Kim, H. S.; Lee, W.; Nam, S. H.; Lee, S.; Yoon, H.; Kim, J.; Yoo, S.; Jeon, S. Quenching-Resistant Solid-State Photoluminescence of Graphene Quantum Dots: Reduction of $\pi-\pi$ Stacking by Surface Functionalization with POSS, PEG, and HDA. *Adv. Funct. Mater.* **2021**, *31*, No. 2102741.
(71) Chakravarty, S.; Gogoi, B.; Mandal, B. B.; Bhardwaj, N.; Sarma, N. S. Silk fibroin as a platform for dual sensing of vitamin B12 using photoluminescence and electrical techniques. *Biosens. Bioelctron.* **2018**, *112*, 18−22.
(72) Dutta, P.; Saikia, D.; Adhikary, N. C.; Sarma, N. S. Macromolecular systems with MSA-Capped CdTe and CdTe/ZnS Core/Shell quantum dots as superselective and ultrasensitive optical sensors for picric acid explosive. *ACS Appl. Mater. Interfaces* **2015**, *7*, 24778−24790.
(73) Pan, D.; Maity, S.; Parshi, N.; Ganguly, J. Remarkable solvent tunable aggregation caused quenching for fluorochromic chitosan-based hydrogel. *J. Mol. Liq.* **2021**, *322*, No. 114565.

https://doi.org/10.1021/acsomega.3c01753
ACS Omega 2023, 8, 21914−21928